Journal of Magnetic Resonance **139,** 8–17 (1999)
Article ID jmre.1999.1762, available online at http://www.idealibrary.com on IDEAL®

A W-Band Pulsed ENDOR Spectrometer: Setup and Application to Transition Metal Centers

I. Gromov,*[,1] V. Krymov,† P. Manikandan,* D. Arieli,* and D. Goldfarb*[,2]

*Department of Chemical Physics, Weizmann Institute of Science, Rehovot 76100, Israel; and †Donetsk Physico-Technical Institute, Donetsk 340114, Ukraine

Received December 21, 1998; revised March 12, 1999

The design and performance of a 95 GHz pulsed W-band EPR/ENDOR spectrometer is described with emphasis on the ENDOR part. Its unique feature is the easy and fast sample exchange at 4.2 K for frozen solution and single crystal samples. In addition, the microwave bridge power output is relatively high (maximum 267 mW), which allows the application of short microwave pulses. This increases the sensitivity in echo experiments because of the broader excitation bandwidth and the possibility of employing short pulse intervals, as long as the dead time does not increase significantly with the power. The spectrometer features two microwave and radiofrequency (0.1–220 MHz, 3 kW pulse power) channels and a 6 T superconducting magnet in a solenoid configuration. The magnet is equipped with cryogenic sweep coils providing a sweep range of ±0.4 and ±0.2 T for a center field of 0–4 and 4–6 T, respectively. The spectrometer performance is demonstrated on Cu(II) centers in single crystals, a zeolite polycrystalline sample, and a protein frozen solution.

Key Words: **W-band; pulsed ENDOR; pulsed EPR; high field.**

INTRODUCTION

One of the current frontiers in the field of EPR spectroscopy is high-field (high frequency) EPR (>2.5 T, >70 GHz) spectroscopy (*1–3*). The scope of high-field EPR is broad and it encompasses all the disciplines of EPR spectroscopy, namely, continuous wave (CW) EPR, pulsed EPR, CW electron-nuclear-double resonance (ENDOR), and pulsed ENDOR spectroscopies. Among the advantages offered by high field EPR are the following: (i) High sensitivity that permits measurements of microsize samples such as single crystals of metalloproteins (*4–6*). (ii) Higher resolution that allows separation of paramagnetic centers with only slightly different g values (*7*). (iii) Small g-anisotropies can be determined, and the wider spread of the powder pattern allows orientation-selective ENDOR and electron spin echo envelope modulation (ESEEM) measurements (*8, 9*). (iv) In high spin systems, high order effects that result in increased inhomogeneous broadening are significantly reduced. Examples are the presence of forbidden transitions in the spectrum of Mn(II), $S = \frac{5}{2}$ (*10*) and high order shifts in ENDOR spectra (*11–13*). (v) ENDOR signals from different nuclei are better resolved because of the significantly larger nuclear Zeeman interaction (*14*) and nuclei with low gyromagnetic ratios can be observed even when the hyperfine interaction is small (*5, 12, 14*). At W-band, protons appear at frequencies much higher than other nuclei, and the overlap between weakly coupled protons and strongly coupled ^{14}N, often encountered in X-band ENDOR spectra, is eliminated (*15*). (vi) In the pulsed version of the experiment, the spectrometer dead time is significantly reduced because the pulse ringdown time constant is inversely proportional to the spectrometer frequency (at constant Q). This permits the use of high Q resonators, and relatively high B_1 fields can be obtained with low power (*17*). (vii) It allows straightforward determination of the signs of the hyperfine and the zero field splitting (ZFS) interactions at low temperatures owing to the large population differences of the various EPR energy levels (*1, 12*). This also leads to a simplification of the EPR/ENDOR spectra since fewer transitions are involved.

There are, however, a few disadvantages: increased inhomogeneous broadening due to g-strain, which may lead to EPR spectra with unresolved hyperfine structure. For some applications the small sample size makes sample handling difficult, as in cases where the samples should be prepared under vacuum or when *in situ* experiments are required. In addition, the reduction of the hyperfine enhancement factor for low γ nuclei with large hyperfine couplings, such as directly bound ^{14}N nuclei, requires high radiofrequency (RF) power.

Parallel to the development of high-field EPR, pulsed EPR/ENDOR spectroscopy has witnessed considerable progress. Sophisticated new pulse schemes have been introduced, and there has been a large increase in the applications of various experiments to a wide range of problems in physics, chemistry, and biology (*16, 12*). These experiments require the generation of a number of microwave (MW) and RF pulses, with variable amplitudes, phases, and frequencies. Moreover, these are often combined with elaborate phase cycling schemes. Multidimen-

[1] On leave from MRS Laboratory, Kazan State University, Kazan, 420008, Russian Federation. Present address: Laboratory of Physical Chemistry, ETH, Zurich CH-8092, Switzerland.

[2] To whom correspondence should be addressed. Fax: 972-8-9344123; E-mail: cigoldfa@wis.weizmann.ac.il.

1090-7807/99 $30.00

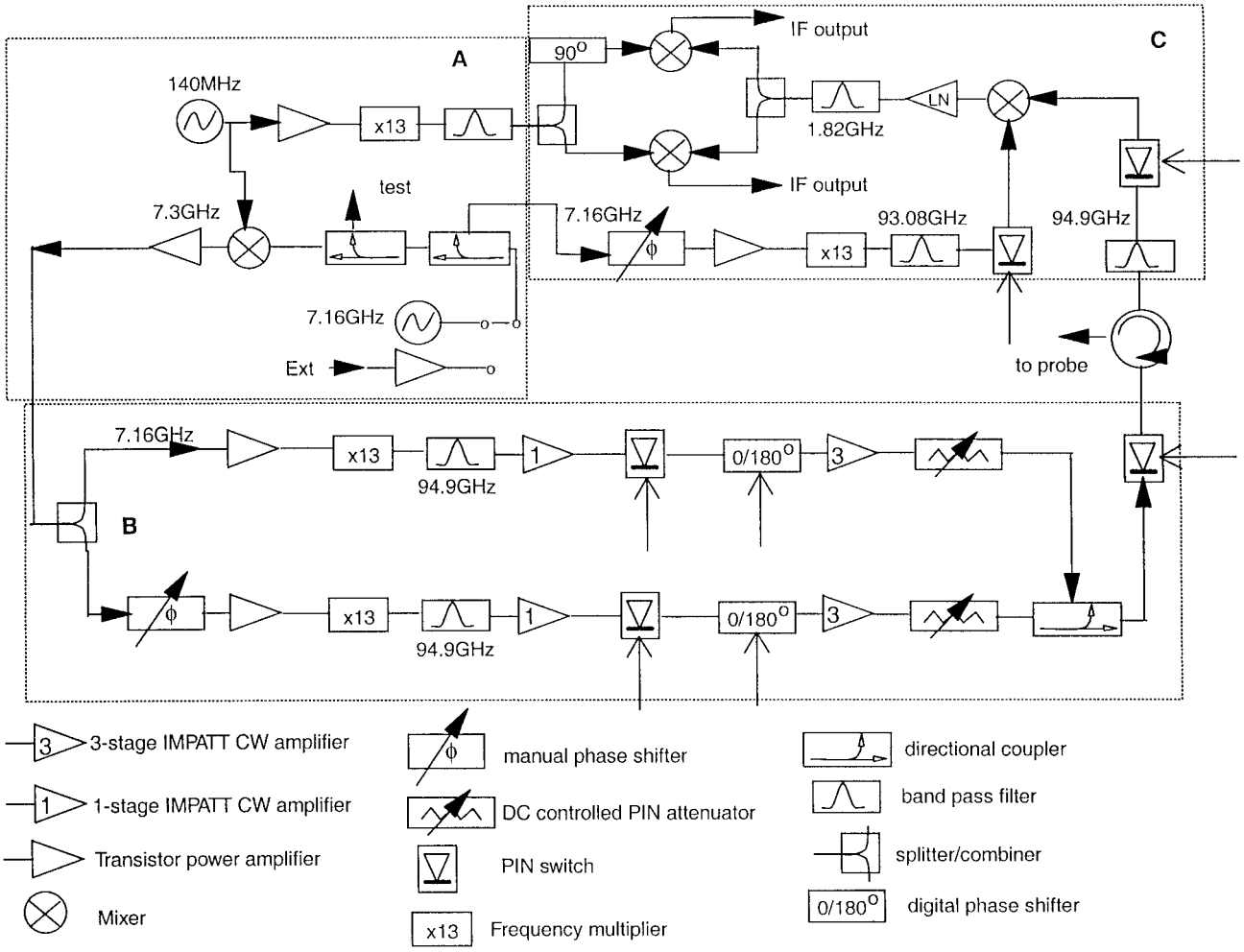

FIG. 1. Block diagram showing the W-band spectrometer microwave bridge. The three boxes A, B, and C correspond to the master frequency source, the receiver, and the transmitter, respectively. The thin arrows represent pulse programmer control.

sional experiments, during which several parameters are varied, such as time intervals, frequency and phase of the MW and RF pulses, and strength of the external magnetic field, B_0, have been designed (*12*). Although the majority of the sophisticated pulse experiments have been demonstrated at X-band frequencies, they are applicable at high fields as well, and therefore high-frequency pulsed spectrometers should exhibit versatility similar to that of modern pulsed X-band spectrometers.

The design and performance of two 95 GHz pulsed EPR/ENDOR spectrometers have been reported so far (*18, 19*), and a number of recent high-field pulsed ENDOR applications, primarily involving organic radicals and metal ion centers in single crystals, have demonstrated the great potential of the method. In this work we describe the pulsed W-band EPR/ENDOR spectrometer setup at the Weizmann Institute with emphasis on the ENDOR part. Its performance is demonstrated on Cu(II) centers in a single crystal, a zeolite polycrystalline sample, and a protein frozen solution. Its unique feature is the easy and fast sample exchange at 4.2 K for frozen solution and single crystal samples. In addition, the MW bridge power output is relatively high, allowing the application of relatively short MW pulses, thus increasing the excitation bandwidth.

EXPERIMENTAL SETUP

The pulsed spectrometer, which can generate hundreds of MW and RF pulses, consists of several parts: a superconducting magnet system, probehead, microwave bridge, pulse programmer, RF system, detection electronics, and a computer. The last four parts are shared with our X-band pulsed EPR/ENDOR spectrometer described earlier (*20*). The pulse programmer is constructed from a word generator (Interface Technologies RS690, 250 MHz) with 32 channels when operating at 4 ns resolution, or 128 channels for 16 ns resolution, coupled to five digital delay generators (Stanford Research Systems DG535). The latter can produce a total of 10 pulses with a time resolution better than 1 ns. The RF system is based on a PTS310 synthesizer (0.1–310 MHz) and an IFI 436P RF am-

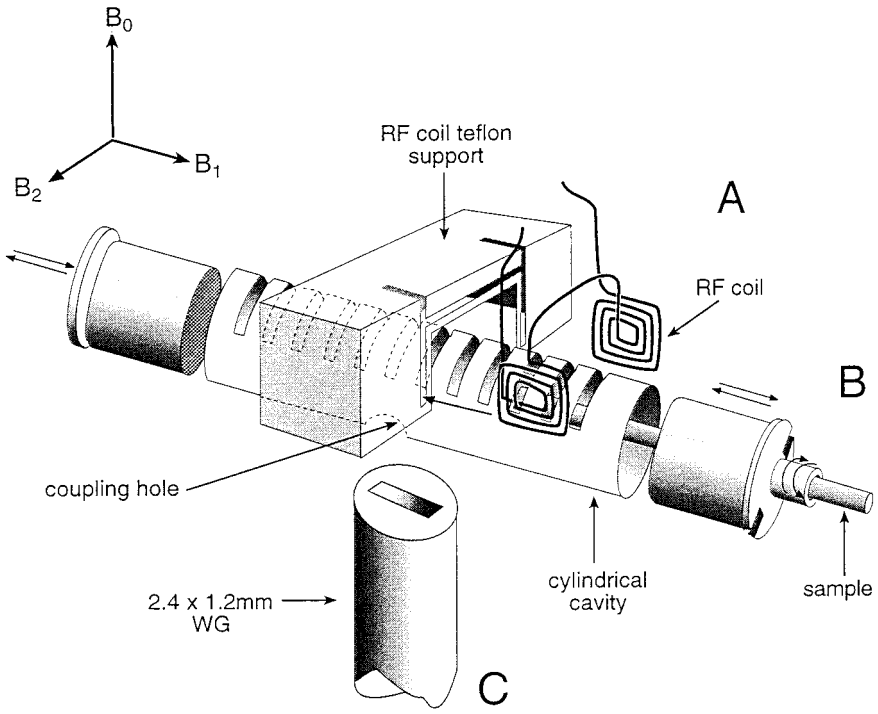

FIG. 2. A schematic arrangement of the MW cavity, the RF coil (A), the plungers used for the cavity tuning, sample position, and sample rotation (B), and the coupling waveguide (C).

plifier (0.01–220 MHz, 3 kW pulse power). The RF circuit is terminated with a 50 ohm load, and a capacitor of 3000 pF is connected immediately after the RF amplifier and acts as a high pass filter. The signal detection electronics includes a video amplifier and a boxcar integrator. The computer used is a Pentium PC and the devices are interfaced to the computer via GPIB, PC-DIO-96, and DAS1200 cards. The software driving the spectrometer is the same as that used for the X-band spectrometer (*20*). In the following, the parts that are unique to the W-band spectrometer will be described in detail.

Magnet

The static magnetic field, B_0, is produced by a solenoid superconducting magnet (Cryomagnetics, Inc). The field can be swept from 0 to 6 T using main current leads that are removable. It can be locked in persistent mode and the leads can be removed to reduce the He consumption. In addition, it includes permanent superconducting sweep coils that allow for sweeps of ± 0.4 and ± 0.2 T for center fields of 0–4 and 4–6 T, respectively. A maximum sweep range requires current of 14.35 A. The homogeneity of B_0 without current in the sweep coils is quoted as ± 0.3 ppm over $1 \times 1 \times 4$ mm^3, which is somewhat larger than the size of a typical sample. When used in the manual mode the power supply resolution is 0.01 A, which amounts to 0.28 mT for the sweep coils. This also determines the stability of the magnetic field when the sweep coils are used, as it was further verified by measurements of the linewidth of a difluoranthenyl phosphorhexafluoride ($(FA)_2^+PF_6^-$) single crystal. A width of 8 MHz was obtained from Fourier transformation of the FID following a $\pi/2$ microwave pulse. The reported linewidth of such a single crystal is 0.001 mT (*21*). In principle, the power supply resolution and stability can be improved to 1.5 mA (0.04 mT for the sweep coils) by using the 16 bit computer interface module (model CIM-16HR).

The magnet has a warm bore of 90 mm diameter fitted with a Janis model STVP-200 "Supertran" variable temperature insert (VTI) (1.4–300 K) with a sample tube inner diameter of 49 mm. A fast direct reading of the magnetic field is afforded by a calibrated meter based on a Hall probe located at a position ($Z = 0$, $R = 18.7$ cm) where the sensed field is proportional to the magnetic field at the sample position ($Z = 0$, $R = 0$). An accurate determination of B_0 in the range of 2.9 to 3.3 T is obtained via the proton Larmor frequency determined from the ENDOR spectra of a frozen solution of a Cu(II)–histidine complex recorded along the EPR powder pattern.

The liquid He consumption is 40–50 ml/h when the main current leads are out and there is no current in the sweep coils. This changes to an average of 60–70 ml/h when there is a current in the sweep coils. With full current in the main coil the He consumption quoted is 450 ml/h.

Microwave Bridge

A block diagram of the microwave bridge, designed and built at Donetsk Physico-Technical Institute, is shown in Fig.

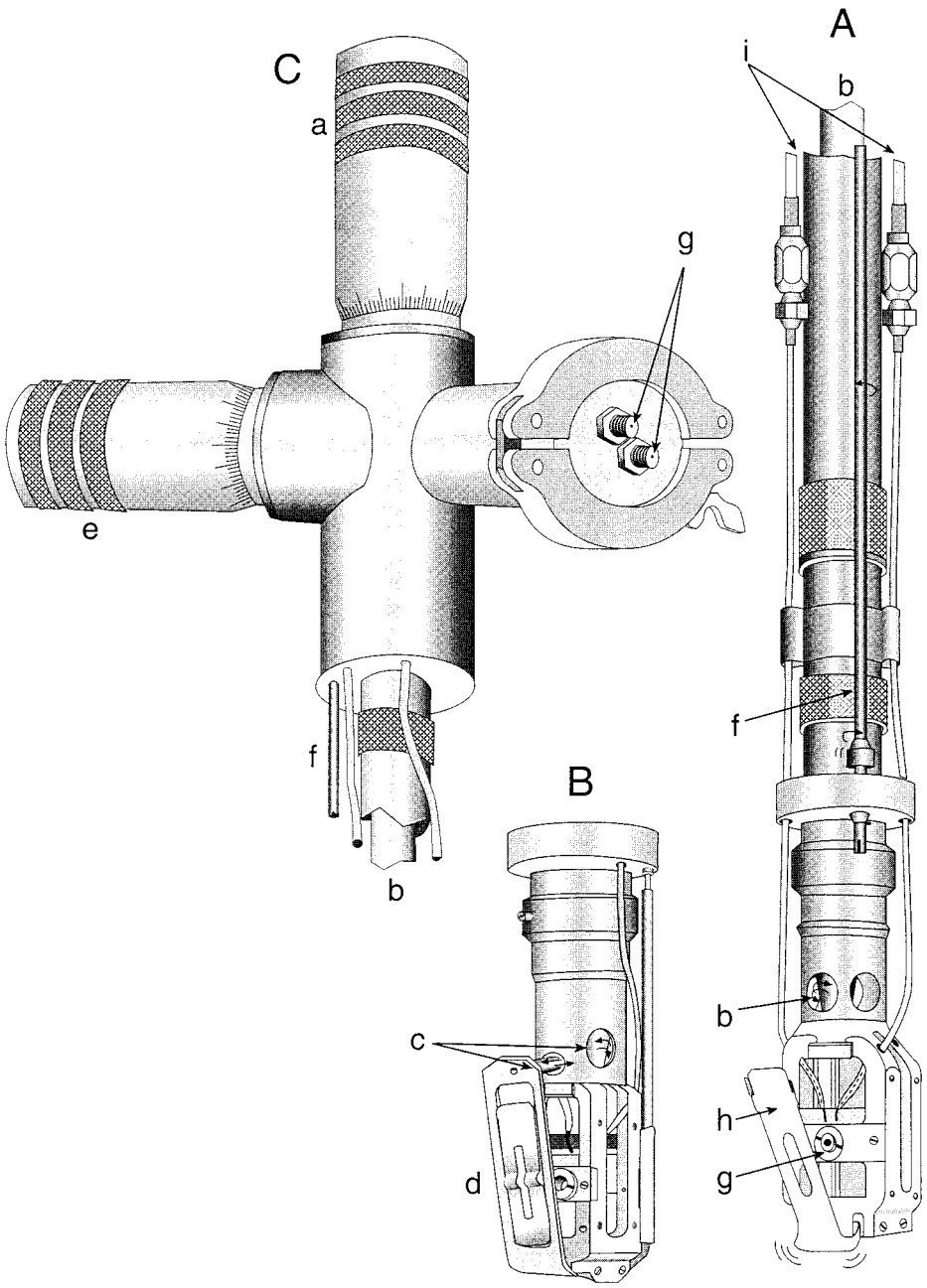

FIG. 3. The internal part of the probehead. (A) Front view of the bottom part, (B) back view of the bottom part, (C) top part. (a) Micrometer knob for cavity tuning, (b) movable rod with a cone at the end (c) that pushes lever (d), (e) micrometer knob for sample rotation, (f) rod for sample rotation mechanism, (g) sample holder, (h) sample clamp, (i) RF cables.

1. It operates at 94.9 GHz and has two channels, one with a maximum power of 120 mW and the other with 29 mW. The second channel can operate in continuous-wave mode as well. Since the two channels are locked to one master oscillator, when their outputs are combined they interfere to give a total power of 267 mW.[3]

[3] This value was obtained by summing the amplitudes of each channel, $(\sqrt{120} + \sqrt{29})^2$.

The base frequency of the bridge is 7.16 GHz, supplied by an internal or external source. This is further mixed with a 140 MHz signal from a reference crystal oscillator to yield a frequency of 7.3 GHz. This CW signal is split into two channels and upconverted by a factor of 13 using an IMPATT CW frequency multiplier in each channel. Some power gain is achieved by a one-stage CW IMPATT amplifier and then the signal is fed into a high speed PIN switch and a 1 bit phase

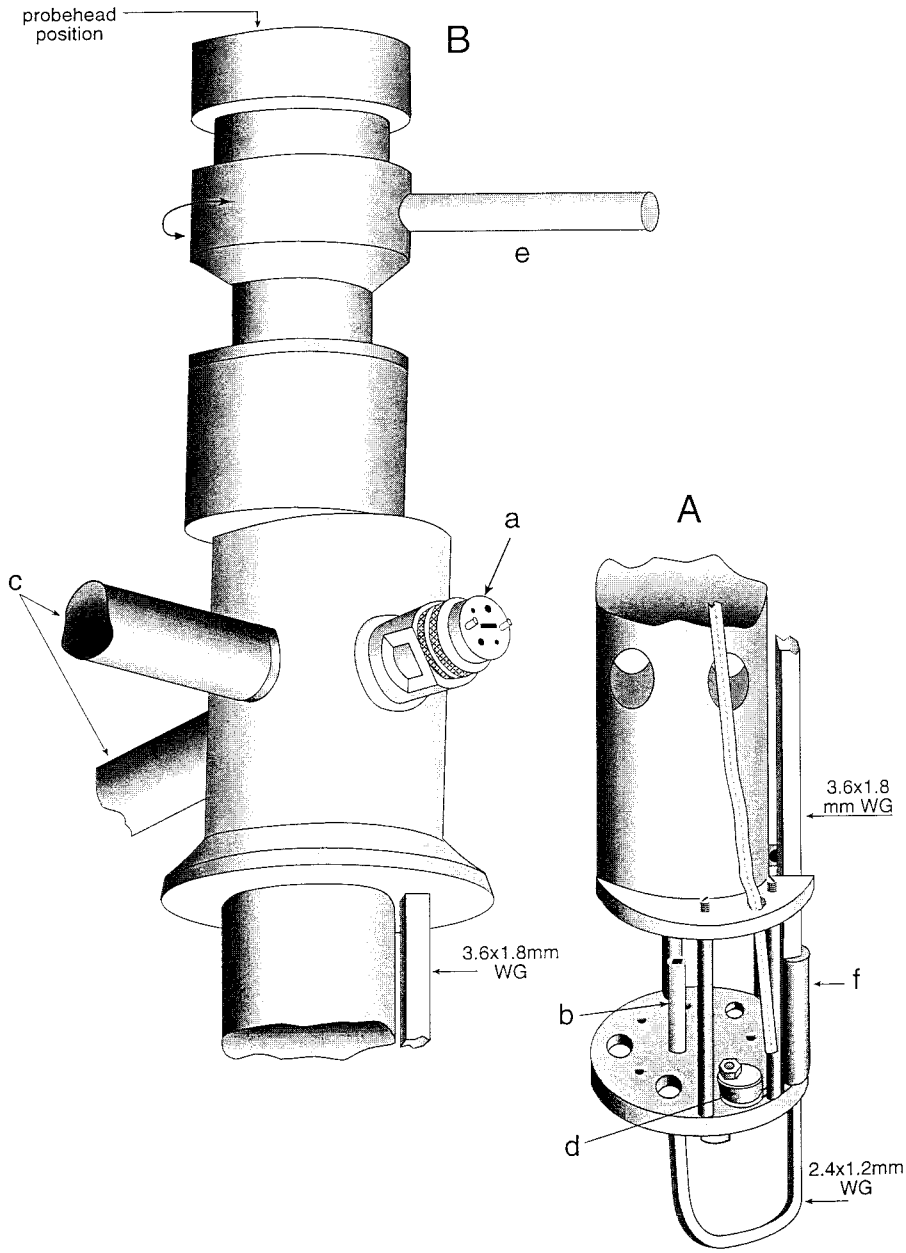

FIG. 4. External part of the probehead. (A) bottom part, (B) top part. (a) Waveguide connection to the MW bridge connection, (b) coupling waveguide, (c) provisions for electrical connections for temperature sensors and (d) a temperature sensor, (e) rod for rotation of the internal part of the probehead for coupling adjustment, (f) a straight transition from 2.4×1.2 mm^2 waveguide to 3.6×1.8 mm^2 waveguide.

shifter. Additional power gain is then obtained by a three-stage CW IMPATT amplifier. The last component in each channel is a dc current controlled PIN attenuator, after which the signals are combined and fed via another high speed PIN switch (5 ns switching time) into the circulator and the cavity. In the receiver the signal is first mixed with a 93.08 GHz signal (obtained by multiplication of the 7.16 GHz source signal by a factor of 13) yielding an intermediate frequency (IF) of 1.82 GHz. This signal is split and one part undergoes a 90° phase shift for quadrature detection. The two signals are finally mixed with a reference 1.82 GHz signal (obtained from the 140 MHz signal after a 13-fold multiplication) to yield the final intermediate (IF) signal outputs. These are amplified, fed into a variable attenuator that is needed when signals are too intense, and finally directed into a boxcar integrator.

The master oscillator in the internal mode is a transistor oscillator stabilized by locking to the resonance frequency of a high Q dielectric resonator. The temperature dependent instability of the master oscillator is 7–8 kHz/degree, and for 1–1.5° this amounts to 100–150 kHz instability at 94.9 GHz.

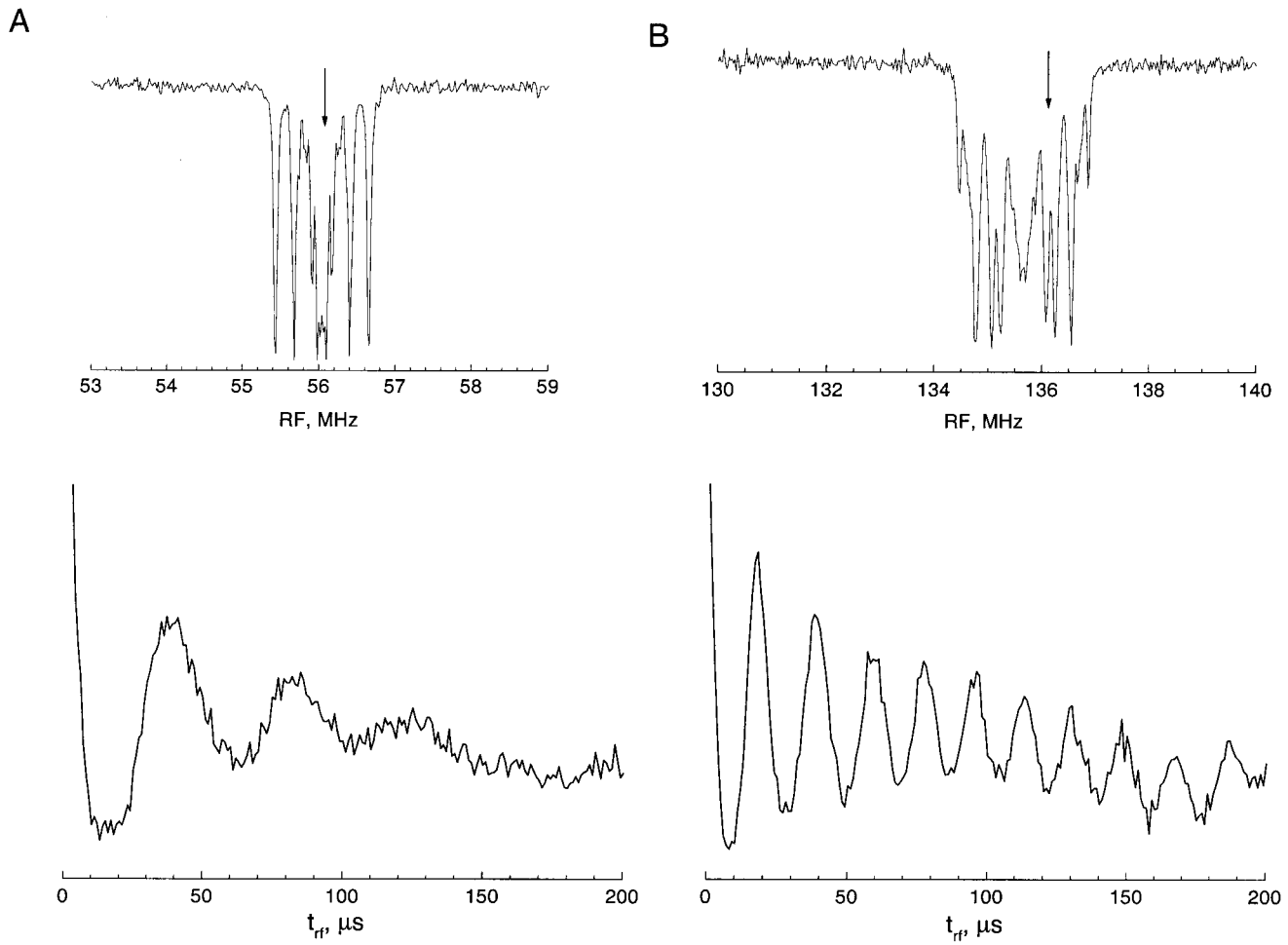

FIG. 5. Rabi oscillations of the ENDOR lines of a γ-irradiated single crystal of LiF, obtained using the Mims ENDOR sequence and recorded at room temperature. (A) ^{7}Li ENDOR spectrum and nutation pattern for the 56 MHz line; (B) ^{19}F ENDOR spectrum and nutation pattern for the 136 MHz line. The microwave pulse length was 60 ns, $\tau = 200$ ns, and $B_0 = 3.381$ T. The positions where nutation patterns were obtained are indicated by arrows on the ENDOR spectra. The RF pulse length in these measurements was 70 μs.

The total noise figure of the receiver at the output point, 10–11 dB, is determined primarily by the noise figures of the balanced mixer (1–2 dB) and the low noise amplifier (7–9 dB). The bandwidth and gain of the latter are 0.1–1.0 GHz and 40–44 dB, respectively. The high-speed PIN diode switch in the receiver has a bandwidth of 2–4 GHz, an insertion loss of 1.5–2 dB, and an isolation of 30–40 dB; its rise time is 3–4 ns.

The Probehead

The cavity used for ENDOR measurements is a cylindrical TE_{011} cavity similar to that described earlier (*8, 18*). It is made out of a brass tube plated with silver and a flash of gold. Its inner diameter is 4.2 mm, its total length is 14.4 mm, and it has 12 slits of 0.2 mm, 0.2 mm apart, to allow RF penetration (see Fig. 2). The coupling hole is of 0.9 mm diameter and the RF coil, which is a four-turn saddle coil made out of a copper wire, is housed in a Teflon holder around the cavity. The coupling is optimized by rotating the cavity with respect to the waveguide. Tuning is achieved by variation of the length of the cavity using a plunger that is made out of a silver/gold plated brass frame. A similar plunger, filled with Rexolite, is located at the other end of the cavity and functions as a sample holder. It can be rotated about the axis of the cavity, perpendicular to the magnetic field, for single-crystal measurements. With the plungers in, the length of the cavity is 3.8 mm. Although the MW bridge is situated at the top of the magnet, very close to the magnet bore opening, the distance between the bridge output and the cavity, 115 cm, is relatively large because of the magnet height. This leads to an approximate power loss of 3 dB. The loss is minimized by using for most of this distance an oversized waveguide.

With full output power of the bridge (267 mW at the bridge output and 120 mW at the cavity) the shortest $\pi/2$ pulse obtained is 40 ns. This corresponds to a B_1 of 0.22 mT. Using B_1 =

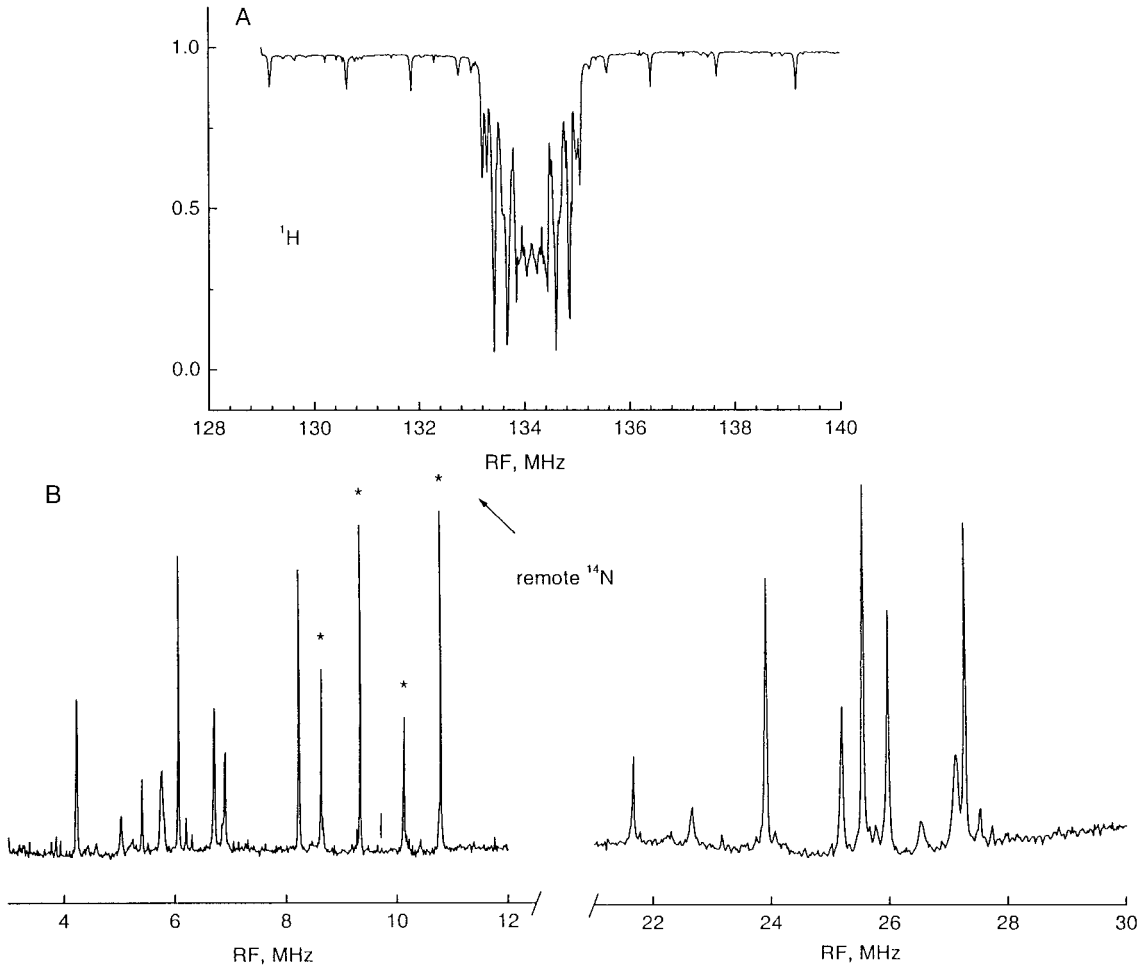

FIG. 6. ENDOR spectra of a single crystal of Cu(II)-doped L-histidine hydrochloride. (A) ^{1}H Mims ENDOR spectrum; t_{MW} = 100 ns; τ = 300 ns; t_{RF} = 35 μs; T = 4.2 K. (B, C) ^{14}N and ^{35,37}Cl Davies ENDOR spectra; t_{MW} = 200, 100, 200 ns; τ = 500 ns; t_{RF} = 100 μs; T = 3.2 K. In all spectra B_0 = 3.15 T and the repetition rate was 50 Hz. Asterisks mark the lines of a remote nitrogen centered around the Larmor frequency of ^{14}N (marked with a vertical solid line).

$c(Q_L P_{MW})^{1/2}$, $Q_L \approx 1000$, $P_{MW} \approx 120$ mW, we obtain a conversion factor c of 0.02 mT/W$^{1/2}$, which is close to the conversion values reported by Prisner *et al.* for their ENDOR probe at 95 GHz (*19*). With full power the spectrometer deadtime is 25 ns.

The probehead consists of two parts, internal and external. The internal part, shown in Fig. 3, houses the cavity ensemble (Fig. 2), the RF coil and cables, and the tuning and sample rotation mechanisms, which were adapted from the design of Lebedev (*2*). The whole internal part is easily removed for sample exchange. Tuning is afforded by rotating a micrometer situated at the top of the probehead (Fig. 3, a), which pushes in and out a conical rod (b, c). This movement regulates a spring (d) that pushes the tuning plunger in and out (Fig. 2). This procedure can be carried out at any measurement temperature. For single-crystal measurements the sample rotation is done through a goniometer (e), which rotates a rod (f), the motion of which is translated to the sample holder (g). The last is not shown in Fig. 3 for the sake of simplicity. The sample holder is held using a cover (h).

The external part of the probe, Fig. 4, into which the internal part is inserted, is situated "permanently" in the sample tube of the Janis VTI. It includes the waveguide connection to the microwave bridge (Fig. 4, a), the waveguide that couples to the cavity (b), provisions for temperature sensors (c, d), and a handle for rotating the internal part with respect to the fixed external part for optimizing the coupling (e). A spring situated at the connection of the bottom part of the internal part and the main supporting rod ensures a good contact between the cavity and the coupling waveguide. This probehead design allows facile and fast sample exchange also at 4.2 K.

PERFORMANCE AND EXAMPLES

Sensitivity

A convenient description of the sensitivity of a pulsed EPR spectrometer has been given by Prisner (*22*). It uses S/N of a

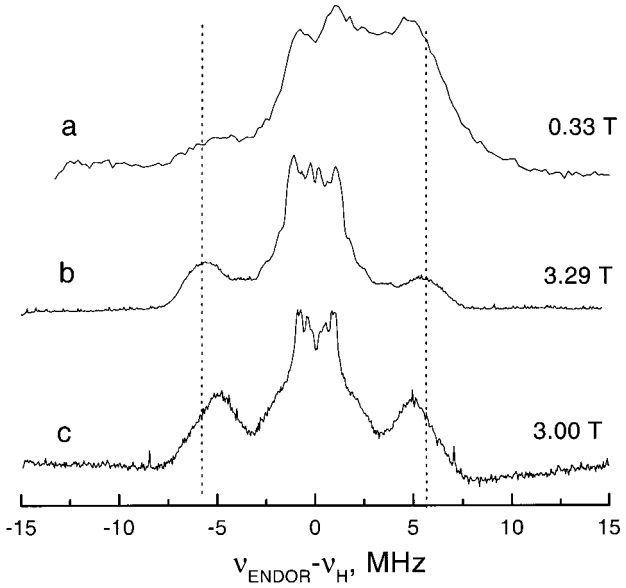

FIG. 7. Davies ENDOR spectra of a powder of Cu(II)–histidine complex encapsulated in zeolite Y. (a) X-band spectrum; $t_{MW} = 200, 100, 200$ ns; $\tau = 500$ ns; $t_{RF} = 6$ μs; repetition rate 500 Hz; $B_0 = 0.33$ T; $T = 4.2$ K. (b) W-band spectrum; $t_{MW} = 180, 90, 180$ ns; $\tau = 400$ ns; $t_{RF} = 20$ μs; repetition rate 100 Hz; $B_0 = 3.29$ T; $T = 5$ K. (c) Same as (b), with $B_0 = 3.0$ T.

single shot, room temperature two-pulse echo signal of a sample with a known number of spins and with a broad inhomogeneous linewidth (broader than the pulse bandwidth). Accordingly, the sensitivity E' is defined as

$$E' = \frac{N}{\Delta B_{1/2} S/N}\, e^{(-2\tau/T_m)}, \qquad [1]$$

where N is the number of spins in the sample, $\Delta B_{1/2}$ is the inhomogeneous linewidth, τ is the time interval between the two pulses, and T_m is the phase memory time. S/N is the signal-to-noise ratio as measured at the maximum echo amplitude. The factor $e^{(-2\tau/T_m)}$ takes the relaxation occurring during 2τ into consideration. In Eq. [1] the S/N is defined under conditions of a detection bandwidth, $\Delta\nu_{det}$, matched to the echo shape given by the excitation bandwidth ($\Delta\nu_{ex} = 1/t_p$). Although this condition can be easily satisfied, $\Delta\nu_{det}$ is often fixed, as in our spectrometer. In this case the S/N at matched condition can be calculated using

$$S/N = \frac{2\sqrt{2}S}{N_{pp}} \left(\frac{\Delta\nu_{det}}{\Delta\nu_{ex}}\right)^{1/2}. \qquad [2]$$

In Eq. [2], S is the signal amplitude and N_{pp} is the noise peak to peak amplitude measured with a bandwidth $\Delta\nu_{det}$. The sample we used was 0.2 mg coal with 2.4×10^{16} spins and $T_m = 0.48$ μs. The number of spins was calibrated against a single crystal of $CuSO_4$, which exhibits a singlet with unresolved hyperfine structure due to spin exchange. The coal sample occupied ~1 mm at the end of a 0.7 mm o.d., 0.5 mm i.d. quartz capillary that was placed in the center of the cavity such that all spins were in the active volume of the cavity. From a single shot of a two-pulse sequence with pulses of 60 and 120 ns (using only channel I) and $\Delta\nu_{det} = 200$ MHz, we obtained $S/N_{pp} = 29$. This yields $E' = 1 \cdot 10^{12}$ spins/G for the ENDOR probehead at room temperature. We carried out similar sensitivity measurements on our X-band pulsed spectrometer using a Britt–Klein (*23, 24*) type cavity and 5.38 mg of the same coal and obtained $E' = 4 \times 10^{14}$ spins/G. The higher sensitivity at W-band, in terms of minimum detected spins, is, however, only relevant to samples with restricted sizes, such as single crystals. When the size is not limited, X-band may be somewhat more sensitive (*19*).

RF Performance

The B_2 field was determined from the Rabi oscillations measured using the Mims ENDOR sequence, $\pi/2$–τ–$\pi/2$–T–$\pi/2$–τ–echo, where an RF pulse is introduced during the T interval. In these measurements the RF frequency was set to one of the ENDOR transitions and the echo intensity was measured as a function of the RF pulse length. The sample of choice was a γ-irradiated LiF single crystal, and the ^{7}Li and ^{19}F regions of the Mims ENDOR spectra are shown in Fig. 5. The experiment was carried out at room temperature on a ^{7}Li (Fig. 5A) and a ^{19}F (Fig. 5B) lines. B_2 fields of 1.2 mT ($t_\pi = 23$ μs) and 1.3 mT ($t_\pi = 10$ μs) were obtained, respectively. The RF pulse power applied in these measurements was 1.2 kW for the ^{19}F measurement and 2 kW for the ^{7}Li measurement, indicating a better conversion factor for the higher frequency range.

Examples

A severe problem of X-band ENDOR is the overlap of weakly coupled protons with doublets centered around the Larmor frequency (14–15 MHz) and strongly coupled ^{14}N nuclei with hyperfine couplings of 20–40 MHz. For example, in the X-band ENDOR spectrum of a Cu(II) doped L-histidine hydrochloride (Cu–His) single crystal, some of the ^{1}H peaks appear in the region of the ^{14}N signals (*25*), while in the W-band spectrum they are very well separated, as shown in Fig. 6. Figure 6A shows the ^{1}H region of a Mims ENDOR spectrum of a single crystal of Cu–His recorded at 4.2 K. The RF π pulse was relatively long, 35 μs, to achieve high resolution. The ^{14}N and ^{35,37}Cl region of a Davies ENDOR of this crystal, recorded at 3.2 K, is shown in Fig. 6B. A rather long RF pulse was required because of the low value of ^{14}N and the significant reduction of the hyperfine enhancement factor at 95 GHz. The ^{14}N signal of the remote nitrogen in the imidazole ring is identified by asterisks in the figure.

The next example is of a polycrystalline sample of a Cu(II) (histidine)$_2$ complex encapsulated in the cages of zeolite Y (*26*). Figure 7 shows a comparison of a Davies ENDOR

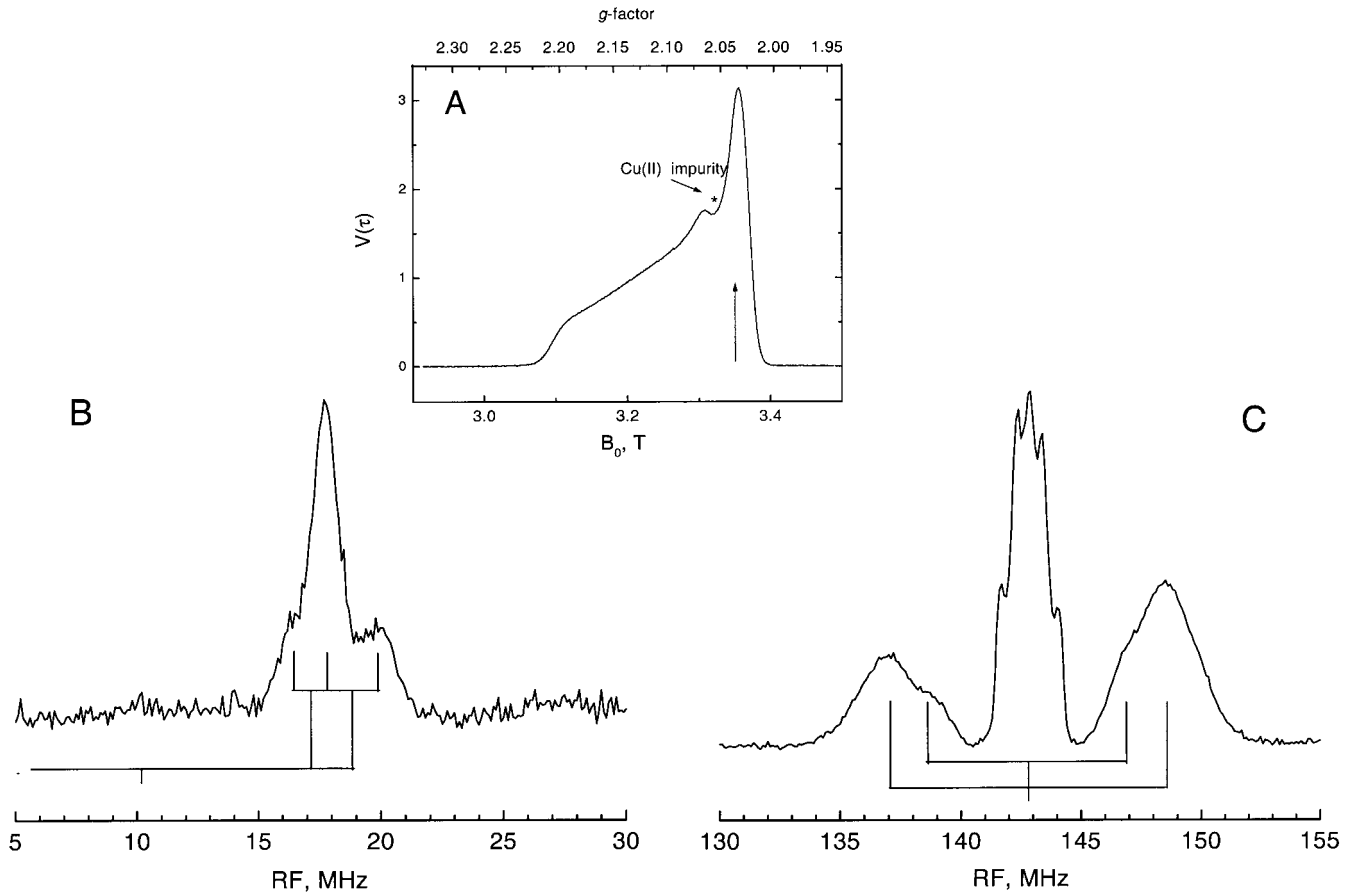

FIG. 8. (A) Echo-detected EPR spectrum of a frozen solution of the M227Q mutant of the soluble Cu_A fragment of cytochrome *c* oxidase; t_{MW} = 90, 180 ns; τ = 340 ns; repetition rate 200 Hz; T = 4.4 K. (B) ^{14}N Davies ENDOR spectrum; t_{MW} = 200, 100, 200 ns; τ = 400 ns; t_{RF} = 50 μs; repetition rate 100 Hz; B_0 = 3.35 T; T = 3.2 K. (C) ^{1}H Davies ENDOR spectrum; t_{MW} = 180, 90, 180 ns; τ = 400 ns; t_{RF} = 10 μs; repetition rate 103 Hz; B_0 = 3.35 T; T = 3.2 K.

spectrum, recorded at the $g_\perp$ position, at X-band and W-band. At X-band the ^{1}H signals are obscured by broad ^{14}N signals in the region of 15–20 MHz, whereas very nice proton powder patterns are observed at the W-band spectrum. The lower trace in Fig. 7 shows the W-band spectrum recorded at the $g_\parallel$ position where a significant decrease in the outer most doublet is evident. The Cu(II) content of this sample is 0.8 Cu(II) per unit cell (4.7×10^{-5} mol/g) and the sample weight was $\sim$1 mg.

The final example is of a frozen solution of the M227Q mutant (1–2 mM) of the Cu_A soluble fragment of cytochrome *c* oxidase (*27*). This protein contains a mixed-valent binuclear copper site with S = $\frac{1}{2}$. In the native protein each of the two copper atoms is coordinated to two bridging cysteine sulfurs and to one histidine residue (*28*). In addition, one copper is coordinated to a methionine sulfur and the other to the peptide carbonyl of a glutamic acid residue. In this particular mutant the methionine has been replaced with glutamine. The echo-detected EPR spectrum is shown in Fig. 8A, and the field at which the ENDOR experiment was performed is marked with an arrow. The ^{1}H Davies ENDOR spectrum, Fig. 8C, indicates the presence of two protons with couplings of 7.9 and 11.6 MHz corresponding to the β protons of the cysteine residues. In the ^{14}N region, (Fig. 8B) signals corresponding to the high field components of two doublets, centered about the Larmor frequency of ^{14}N, appear. From these lines hyperfine couplings of 17.6 and 13.2 MHz, with quadrupolar splittings of 2 and 1.2 MHz, respectively, are estimated.

SUMMARY

A 95 GHz pulsed ENDOR spectrometer, featuring a probe-head for fast sample exchange at low temperatures, has been constructed. Using a high power RF amplifier and a non-matched RF circuit it is possible to measure broadband ENDOR spectra with signals ranging from ^{14}N to ^{1}H at temperatures of 4.2 K and below. This was demonstrated on Cu(II) centers in a single crystal, polycrystalline oxide, and protein frozen solution.

ACKNOWLEDGMENTS

This research was supported by the MINERVA Foundation. We thank Prof. J. Schmidt and Dr. O. Poluektov for much helpful advice and the gift of the LiF sample. The help of Y. Saranga, Y. Gorodeski, and J. Zibziner in the probe design and construction and the setup of the required electronics is greatly appreciated. We thank Dr. C. Slutter for the M227Q mutant and Dr. B. M. Weckhuysen for the Cu(histidine)$_2$ encapsulated zeolite Y sample. The support of the Gerhard M. G. Schmidt Minerva Center for Supramolecular Architecture is greatly appreciated.

REFERENCES

1. Ya. S. Lebedev, *in* "A Specialist Periodical Report, Electron Spin Resonance" (N. M. Atherton, Ed.), Vol. 14, pp. 63–87, The Royal Society of Chemistry (1994).
2. Ya. S. Lebedev, in "Modern Pulsed and Continuouse-Wave Electron Spin Resonance" (L. Kevan and M. K. Bowman, Eds.), Wiley, New York (1990), pp. 365–404.
3. K. A. Earle, D. E. Budie, and J. H. Freed, *in* "Advances in Magnetic and Optical Resonance" (W. S. Warren, Ed.), Vol. 19, pp. 253–323, Academic Press (1996).
4. J. W. A. Coremans, O. G. Poluektov, E. J. J. Groenen, G. W. Canters, H. Nar, and H. Messerschmidt, *J. Am. Chem. Soc.* **116,** 3037–3101 (1994).
5. J. W. A. Coremans, M. van Gastel, O. G. Poluektov, E. J. J. Groenen, T. den Glaauwen, G. van Pouderoyen, G. W. Canters, H. Nar, C. Hamman, and H. Messerschmidt, *Chem. Phys. Lett.* **235,** 202–210 (1995).
6. J. W. A. Coremans, O. G. Poluektov, E. J. J. Groenen, G. W. Canters, H. Nar, and H. Messerschmidt, *J. Am. Chem. Soc.* **118,** 12141–12153 (1996).
7. T. F. Prisner, A. E. McDermott, S. Un, M. C. Thurnaur, and R. G. Griffin, *Proc. Natl. Acad. Sci. USA* **90,** 9485–9488 (1993).
8. O. Burghaus, M. Plato, M. Rohrer, K. Möbius, F. MacMillan, and W. Lubitz, *J. Phys. Chem.* **97,** 7639–7649 (1993).
9. M. Rohrer, M. Plato, F. MacMillan, Y. Grishin, W. Lubitz, and K. Möbius, *J. Magn. Reson. A* **116,** 59–66 (1995).
10. B. F. Bellew, C. J. Halkides, G. J. Gerfen, R. G. Griffin, and D. J. Singel, *Biochemistry* **35,** 12186–12193 (1996).
11. D. Goldfarb, M. Bernardo, K. G. Strohmaier, D. E. W. Vaughan, and H. Thoamann, *in* "Zeolites and Related Microporous Materials, State of the Art 1994" (J. Weitkamp, H. G. Karger, H. Pfiefer, and W. Hölderich, Eds.), Studies in Surface Science and Catalysis, Vol. 84, pp. 403–412, Elsevier (1994).
12. D. Goldfarb, O. Poluektov, J. Schmidt, K. G. Strohmaier, D. E. W. Vaughan, and H. Thomann, *J. Am. Chem. Soc.* **181,** 4665–4671 (1996).
13. B. E. Sturgeon, J. A. Ball, D. W. Randall, and R. D. Britt, *J. Phys. Chem.* **98,** 12871–12883 (1994).
14. M. T. Bennebroek, O. G. Poluektov, A. J. Zakrzewski, P. G. Baranov, and J. Schmidt, *Phys. Rev. Lett.* **74,** 442–445 (1995).
15. M. M. Werst, C. E. Davoust, and B. M. Hoffman, *J. Am. Chem. Soc.* **113,** 1533–1538 (1991).
16. C. Gemperle and A. Schweiger, *Chem. Rev.* **91,** 1481–1505 (1991).
17. T. F. Prisner, S. Un, and R. G. Griffin, *Isr. J. Chem.* **32,** 357–363 (1992).
18. J. A. J. M. Disselhorst, H. van der Meer, O. G. Poluektov, and J. Schmidt, *J. Magn. Reson. A* **115,** 183–188 (1995).
19. T. F. Prisner, M. Rohrer, and K. Möbius, *Appl. Magn. Reson.* **7,** 167–183 (1994).
20. J. J. Shane, I. Gromov, S. Vega, and D. Goldfarb, *Rev. Sci. Instrum.* **69,** 3357–3364 (1998).
21. R. T. Weber, J. A. J. M. Disselhorst, L. J. Prevo, J. Schmidt, and W. Th Wenckbach, *J. Magn. Reson.* **81,** 129–144 (1989).
22. T. F. Prisner, *Adv. Magn. Opt. Reson.* **20,** 245–299 (1997).
23. R. D. Britt and M. P. Klein, *J. Magn. Reson.* **74,** 535–540 (1975).
24. D. Goldfarb, J. M. Fauth, Y. Tor, and A. Shanzer, *J. Am. Chem. Soc.* **113,** 1941–1948 (1991).
25. C. A. McDowell, A. Naito, D. L. Sastry, Y. U. Cui, K. Sha, and S. X. Yu, *J. Mol. Struct.* **195,** 361–381 (1989).
26. B. M. Weckhuysen, A. A. Verbeckmoes, I. P. Vannijvel, J. A. Pelgrims, P. L. Busken, P. A. Jacobs, and R. A. Schoonheydt, *Angew. Chem. Int. Ed. Engl.* **34,** 2652–2654 (1995).
27. C. E. Slutter, D. Sanders, P. Wittung, B. G. Malmström, R. Aasa, J. H. Richards, H. B. Gray, and J. A. Fee, *Biochemistry* **35,** 3387–3395 (1996).
28. (a) S. Iwata, C. Ostermeier, B. Ludwig, H. Michel, *Nature* **376,** 660–669 (1995); (b) T. Tsukihara, H. Aoyama, E. Yamashita, T. Toxizaki, H. Yamaguchi, K. Shinzawa-Itoh, R. Nakashima, R. Yaono, and S. Yoshikawa, *Science* **269,** 1069–1074 (1995).